crystals

MDPI

Article

Engineered Layer-Stacked Interfaces Inside Aurivillius-Type Layered Oxides Enables Superior Ferroelectric Property

Shujie Sun * and Xiaofeng Yin

Collaborative Innovation Center of Henan Province for Energy-Saving Building Materials, Xinyang Normal University, Xinyang 464000, China; yxfeng@xynu.edu.cn

* Correspondence: sjsun@xynu.edu.cn

Received: 13 July 2020; Accepted: 12 August 2020; Published: 18 August 2020

Abstract: Layer engineering with different layer numbers inside Aurivillius-type layered structure, similar to interface engineering in heterojunctions or superlattices, can give rise to excellent physical properties due to the correlated layer-stacked interfaces of two different layer phases with different strain states. In this work, using the solid-state reactions from Aurivillius-type Bi_3TiNbO_9 (2-layer) and $Bi_4Ti_3O_{12}$ (3-layer) ferroelectric powder mixtures, single-phase compound of $Bi_7Ti_4NbO_{21}$ with an intergrowth structure of 2-layer and 3-layer perovskite slabs sandwiched between the Bi-O layers was synthesized and the effects of this layer-engineered strategy on the structure, Raman-vibration and ferroelectric properties were systematically investigated. The mostly-ordered intergrowth phase was observed clearly by utilizing X-ray diffraction and advanced electron micro-techniques. Uniformly dispersions and collaborative vibrations of Ti and Nb ions in the layer-engineered $Bi_7Ti_4NbO_{21}$ were demonstrated. Remarkably, dielectric and ferroelectric properties were also recorded and an enhanced ferroelectric response was found in the layer-engineered mixed-layer sample with high ferroelectric Curie temperature, compared with the homogeneous 2-layer and 3-layer samples. Analyses of the Raman spectra and atomic structures confirmed that the performance improvement of the layer-engineered sample is intrinsic to the correlated layer-stacked interfaces inside the Aurivillius-type layered oxides, arising from strain-induced lattice distortions at the interfaces.

Keywords: Aurivillius oxide; ferroelectric; layer engineering; intergrowth; heterogeneous

1. Introduction

Oxide interfaces can produce many novel effects and functions, arising from the reconstruction of the charge, spin and orbital states at interfaces on the nanometer scale, due to the broken symmetries of the order parameters [1]. Over the past decade, in this rapidly emerging field, there has been a burst of activity to manipulate charge and spin orderings, metal-insulator transitions, multiferroic and other phenomena, as well as to create some new ones via interface engineering [2–4]. Recently, extensive reported work has been focused on excellent interface properties in oxide superlattices, for example, atomic-scale layer-by-layer designed ferrimagnetic $LuFe_2O_4$ layers within multiferroic $LuFeO_3$ matrix, $(LuFeO_3)_m/LuFe_2O_4$ superlattices, yield new room-temperature magnetoelectric multiferroic materials [5]. A fundamental basis for understanding the oxide interfaces is strain resulting from the mismatch of lattice parameters, and this strain is accommodated by a combination of lattice deformations and oxygen octahedral rotations, which influence the orbital occupation through the crystal field, leading to novel emergent phenomena that appear through the collective behavior of electrons [6]. In layered perovskites, the complicated layer structure can offer great potential for

tailoring specific properties by varying different ionic compositions or even the number of layers [7]. Normally, the layered structures in Aurivillius, Ruddlesden-Popper and Dion-Jacobson families exhibit the same basic perovskite motif, but the layers of anions and cations may be stacked in multiple ways [8]. In fact, such structural intricacy provides many opportunities to turn and tweak the design, for example, layer-thickness and layer number, multi-selective chemical substitution, and inducing stress-strain applied to the crystal.

Recently, single-phase Aurivillius-type layered ferroelectrics with the general formula $(Bi_2O_2)^{2+}(A_{n-1}B_nO_{3n+1})^{2-}$ have attracted increasing research interest because of their promising electrical properties such as new lead-free piezoelectric materials operating at high temperatures [9]. For example, the well-known $Bi_4Ti_3O_{12}$ (n = 3) compound presented large spontaneous polarization, anisotropy and high Curie temperature [10] and the Bi_3TiNbO_9 (n = 2) compound exhibited the excellent resistance to polarization fatigue [11]. Such layered bismuth-bearing perovskite compounds are alternately stacked with fluorite-type $(Bi_2O_2)^{2+}$ layer and n-layer perovskite-like $(A_{n-1}B_nO_{3n+1})^{2-}$ slabs along its crystallographic c-axis [12]. In analogy to heterostructures and superlattices in thin-film form [8], this special layered architecture is similar to a natural but single-phase superlattice and has many one-dimensional layer-stacked interfaces [12–14]. From this viewpoint, the layer-stacked interfaces may offer a unique and important experimental test-bed. Hereby, if the ability to engineer the layer-stacked interfaces inside Aurivillius-type layered perovskite structures is available, it would be a significant subject to find fascinating phenomena or tailor functional properties.

In general, the layer-stacked interface region inside Aurivillius-type layered structure refers to the region of the nanostructure among the perovskite slabs (average thickness ~ 1.23 nm), including one fluorite-type Bi-O layer and the two perovskite layers adjacent to the sandwiching Bi-O layer [15]. It is known that the Aurivillius-type homogeneous layered oxides with integer n have the same strain states in two sides of the layer-stacked interface due to the same n-layer perovskite slabs. In fact, these structural conditions are unable to highlight the advantages of the interfaces. Fortunately, our recent research has demonstrated the existence of the mixed-layer compounds which are important parts of the Aurivillius-type oxide family with different perovskite layers sandwiched between the Bi-O layers [16–18]. Therefore, the spatial inversion symmetry of the layer-stacked interfaces in the layered structure can be broken by engineering different n-layer perovskite slabs. The polar at the layer-stacked interface would reconstruct through defects and lattice distortions [19,20]. More importantly, on short length scales, the engineered structure can be deemed as the oxide heterostructure and the periodically repeating of engineered heterostructure constitutes an intergrowth structure in the Aurivillius-type layered oxides [21], which is similar to three-tile quasi-periodic superlattices, thus likely giving rise to some excellent properties and novel phenomena. However, until now, much less attention has been paid to studying the layer-stacked interfaces inside Aurivillius-type layered structure. In this work, we exploited such techniques to directly design the intergrowth structure by chemical reaction between two adjacent homogeneous-phase structures, engineering the layer-stacked interface. As an example, the single-phase compound of $Bi_7Ti_4NbO_{21}$ with the intergrowth phase structure of 2-layer and 3-layer perovskite slabs sandwiched between the Bi-O layers was synthesized via traditional solid-state reactions using the prepared powders of Bi_3TiNbO_9 (n = 2) and $Bi_4Ti_3O_{12}$ (n = 3). The effects of the layer-stacked interfaces by layer engineering on the structural, Raman-vibration and ferroelectric property were discussed in details.

2. Experimental Process

Polycrystalline Bi_3TiNbO_9 (BTN-9) and $Bi_4Ti_3O_{12}$ (BTO−12) powders were prepared by traditional solid-state reaction method. Stoichiometric amounts of Bi_2O_3, TiO_2 and Nb_2O_5 as starting materials were mixed and pre-burned at 750 °C for 5 h and then calcined at 1000 °C for BTN-9 and 950 °C for BTO−12, for 2 h in air. A total of 10 mol% of excess Bi was used to compensate the bismuth volatilization under the temperature conditions of either powder synthesis or heating treatments. $SrBi_2Nb_2O_9$ (SBN-9, 2-layer) powders as the reference sample were also prepared using a similar method. Second,

powders of $Bi_7Ti_4NbO_{21}$ (BTNO-21) were first synthesized using the solid-state reactions from BTN-9 and BTO−12 powder mixtures. In most cases, the BTNO-21 synthesized by the traditional solid-state methods directly using Bi_2O_3, TiO_2 and Nb_2O_5 with sintering above 1000 °C usually present some secondary phases. Therefore, the synthesis method in this work was better than some previous reports and the single-phase layer-structural BTNO-21 powders were successfully obtained. Then, the BTNO-21 powders were cold-pressed into pellets with a dimension of 12 mm (diameter) × 2 mm (thickness) and then were sintered in a high-temperature furnace at 1125 °C for 3 h in air to fabricate the dense ceramics (BTN-3 and BTO−12 ceramics sintered at 1100 °C for 3 h).

The crystal phase identification was performed using powder X-ray diffraction (XRD) with Cu-Ka radiation (SmartLab-9kW, JEOL, Tokyo, Japan). Cross-sectional morphologies and atomic structures of the samples were observed using scanning electron microscope (SEM, JSM-S4800, Hitachi, Tokyo, Japan) and high-angle annular dark-field scanning transmission electron microscopy (HAADF-STEM, JEM-ARM200F, JEOL, Tokyo, Japan). Raman spectra were conducted with a Laser Raman spectrometer (LabRam-HR800, Horiba Jobin-Yvon, Paris, France). Chemical states were measured by x-ray photoelectron spectroscopy (XPS, K-ALPHA, ThermoFisher Scientific, London, UK). To measure electric properties, the ceramic pellets were polished to a thickness of 0.3–0.6 mm and Ag was evaporated on both sides as electrodes. A Sawyer-Tower circuit attached to a computer-controlled standardized ferroelectric test system (Radiant Technology Product, Albuquerque, NM, USA) was applied to test ferroelectric property. High-temperature dielectric responses were measured using an impedance analyzer (HP4294A; Agilent Technology, Santa Clara, CA, USA).

3. Results and Discussion

3.1. Crystal Phase and Mixed-Layer Structure

XRD patterns of the BTN-9 and BTO−12 powders synthesized by the solid-state reaction are shown in Figure 1a. Qualitative XRD analyses support the expected Aurivillius-type layered structure in both samples. All of the XRD peaks of the BTN-9 and BTO−12 match well to those of corresponding standard powder diffraction data PDF#39-0233 and PDF#35-0795, respectively. Based on the obtained BTN-9 and BTO−12 powders, the BTNO-21 powders were synthesized using the solid-state reactions from the two powder mixtures. To illustrate the formation process, the crystalline phase of the mixed powders calcined at different temperatures were recorded, as shown in Figure 1b. When the calcination temperature was below 1100 °C, the XRD pattern corresponding to BTN-9, BTNO-21 and BTO−12 can be clearly identified. It can be seen that the peaks from the BTN-9 and BTO−12 become weakened and disappeared with increasing the calcination temperatures, as shown in Figure 1c. The XRD diffraction peaks of the BTNO-21 powders synthesized at 1125 °C/2 h were identified as belonging to the single-phase of the Aurivillius-type intergrowths (PDF#31-0202), indicating that the BTN-9 and BTO−12-based oxides react to form the BTNO-21-based layered oxide, and that the amount of impurity phases, if they exist, is below the XRD's instrumental resolution.

Fabrication of the BTN-9, BTNO-21 and BTO−12 ceramics followed the procedures of cold-pressed forming of the pellets and then no-press sintering of the pellets for ceramics. The cross-sectional SEM images of the three ceramics are shown in Figure 2. The cross-sectional morphologies of all the samples show the plate-like grains, due to the anisotropic nature of the Aurivillius-type crystal structure [15]. Similar dense microstructures with nearly no pores imply that the below-mentioned ferroelectric property could be correlated with the intrinsic crystal structures. To make the atomic layers of the Aurivillius-type intergrowths clearly visualized, the HAADF-STEM images were obtained and are shown in Figure 3. An annotation is that all the orderly arranged bright spots belong to the Bi atoms. Two closely stacked Bi layers in the figures are namely one fluorite-type Bi-O layer and one or two layers of Bi atoms sandwiched by the Bi-O layers, where the Ti/Nb atoms are arranged between these Bi layers, and can be easily understood as corresponding to the 2-layer or 3-layer perovskite-like slabs. Observably, the images in Figure 3 show the Aurivillius-type mixed-layer

structure, characterized by mostly ordered intergrowths of the 2-layer and 3-layer perovskite slabs, which were different with disordered intergrowths of reported $Bi_{11}Fe_3Ti_6O_{33}$ [15], $Bi_9Fe_{5.4}Ti_{2.6}O_{27}$ [18] and $Bi_6Ti_{2.99}Fe_{1.46}Mn_{0.55}O_{18}$ [20]. This means that lots of layer-stacked interfaces engineered by the 2-layer and 3-layer slabs exist in the BTNO-21 material. These engineered layer-stacked interfaces suffered from different strain states, probably resulting in complicated lattice deformations and oxygen octahedral rotations [14]. Furthermore, the X-ray energy dispersive spectrum (EDS) and element mappings of the BTNO-21 were conducted in a selected area, as shown in Figure 4. The atomic ratio of Bi, Ti and Nb is approximately 7: 4: 1, consistent with the formula of $Bi_7Ti_4NbO_{21}$. The nearly uniform distribution of Nb atoms in the 3-layer perovskite slab demonstrated the atomic-scale not reconstructing the atomical layer-insertion into the layered structure for the chemical reactions of the BTN-9 and BTO−12 compounds.

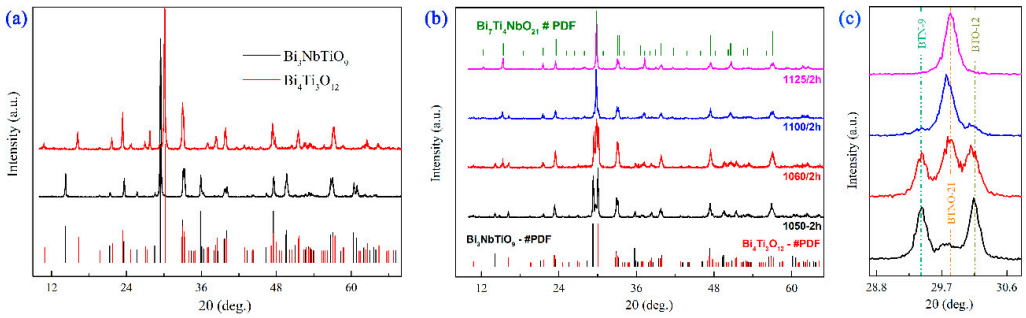

Figure 1. (**a**) Powder X-ray Diffraction (XRD) patterns of Aurivillius-type BTN-9 (n = 2) and BTO−12 (n = 3); (**b**) Powder XRD patterns of the BTNO-21 synthesized using the solid-state reactions from the BTN-9 and BTO−12 powder mixtures at different calcination temperatures; (**c**) The magnified section in the 2θ range 28.7–30.8° in part b. The intensities were normalized and shifted intensities for ease of comparison.

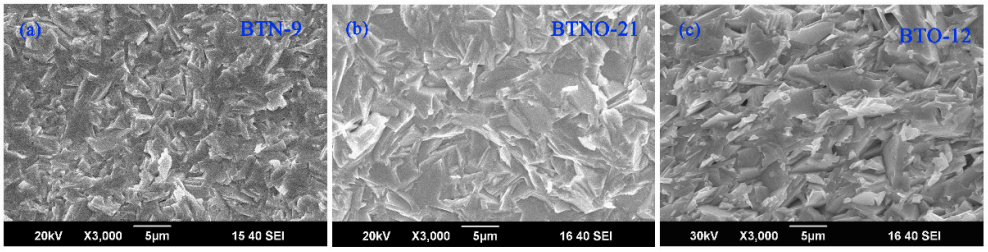

Figure 2. The cross-sectional Scanning Electron Microscopy (SEM) morphologies of (**a**) BTN-9, (**b**) BTNO-21 and (**c**) BTO−12 ceramics.

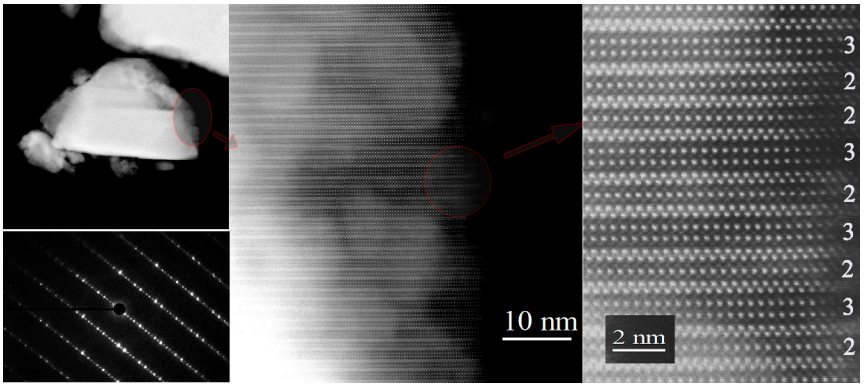

Figure 3. The Transmission Electron Microscopy (TEM), Selected-Area Electron Diffraction (SAED), High-Angle Annular Dark-Field Scanning Transmission Electron Microscopy (HAADF-STEM) images of the BTNO-21.

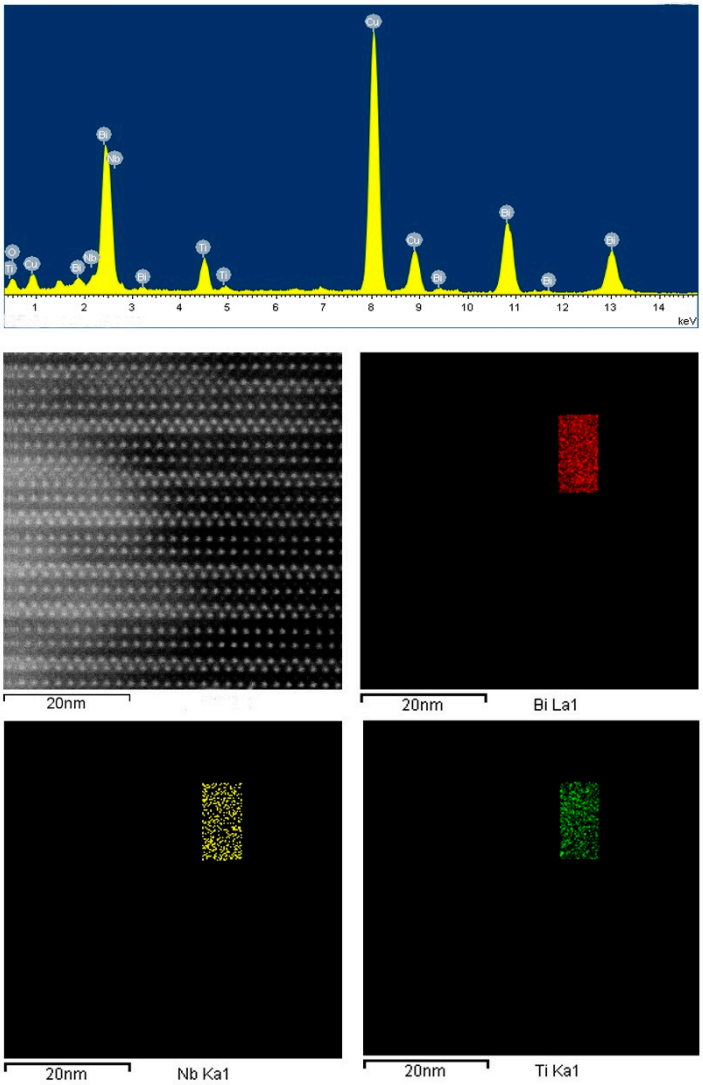

Figure 4. The Energy Dispersive Spectrum (EDS) and element mapping images of Bi, Nb and Ti for BTNO-21 on a selected area.

3.2. Insight from Raman and XPS Spectra

Raman spectroscopy as an important structural analysis technique is always used to distinguish the differences of the closely related structures by taking advantage of its high sensitivity towards metal–oxygen vibrations [22]. Figure 5 shows the Raman spectra of the SBN-9, BTN-9, BTNO-21 and BTO−12 compounds. Here, SBN-9 as the reference sample was prepared to help with the analysis of Raman active modes. In general, for Bi-based layer-structured crystals, the vibration modes below 200 cm^{-1} are ascribed to the vibrations of the Bi^{3+} ions at Bi-O layers or perovskite slabs, and the modes above 200 cm^{-1} result from the octahedral O-B-O and B-O vibrations [23]. In Figure 5a, the mode at ~82 cm^{-1} was attributed to the vibration of the Bi^{3+} ions at the Bi-O layers. However, in all the samples, the intensity of the two modes at ~82 cm^{-1} and ~102 cm^{-1} and the position of the mode at ~102 cm^{-1} show obvious differences. These suggest that the vibrations of the Bi^{3+} ions at the A-sites of the perovskite slabs become stronger and the position of the average vibration may shift toward the high frequencies when the number of layers is increased. The Sr-substitution weakened the vibrations of the Bi^{3+} ions at the perovskite slabs and increased the vibrations of the Bi^{3+} ions at the Bi-O layers, suggesting that chemical doping may be an effective way of modulating the Aurivillius-type structure. In addition, the marked mode (*) below 200 cm^{-1} only existed in the BTN-9 and BTO−12, which is related with the vibrations of the other Bi^{3+} ions at the other equivalent location in the perovskite

slabs. This means that the mixed-layer structure broke some symmetries, then giving rise to the disappearance of some special modes. The major modes of the BTNO-21 at about 222 cm^{-1}, 262 cm^{-1}, 319 cm^{-1} and 360 cm^{-1} (O-Ti-O or O-Nb-O bendings) were similar to those of the BTO−12, while the modes of the BTNO-21 at 500–600 cm^{-1} (Ti-O or Nb-O torsional bendings) were similar to those of the BTN-9. It should also be noted that one or two kinds of metal ions on the B-sites were easily recognized by the modes at 740–910 cm^{-1}, which can be ascribed to the symmetric stretching of the BO_6 octahedra. In Figure 5b, despite that the ratio of Nb/(Ti+Nb) in the BTN-9 is much higher than that in the BTNO-21, the Nb-related vibration compared to corresponding Ti-vibration of the BTNO-21 has a higher intensity than that of the BTN-9. This might be attributed to the distortions from the Nb-O bonds. Concisely, by comparing the modes above 200 cm^{-1} of all the samples, the mixed-layer structure increased the comprehensive vibrations of the Nb-O and Ti-O bonds especially the Nb-O vibrations.

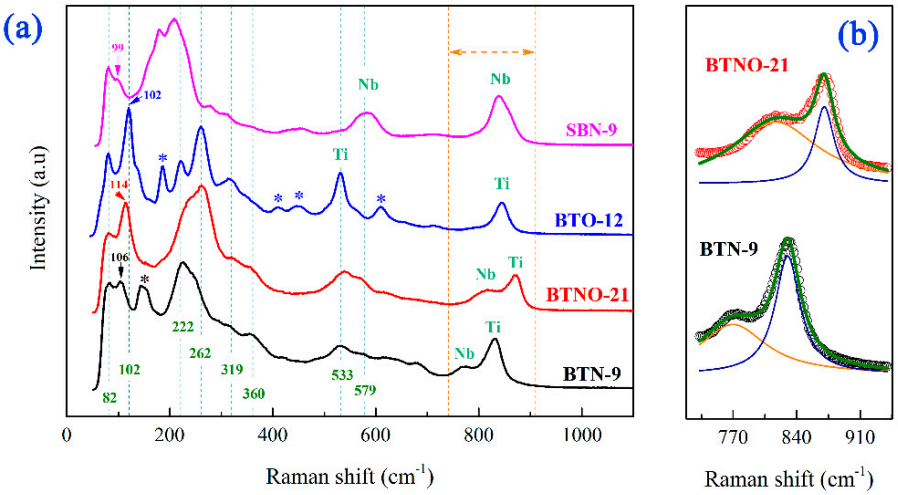

Figure 5. (**a**) Raman spectra of the SBN-9, BTN-9, BTNO-21 and BTO−12; (**b**) The magnified sections of the Raman spectra. The marked modes (*) only belong to the BTN-9 or BTO-12. The broad peak of the BTN-9 and BTNO-21 at 750–910 cm^{-1} was fitted and decomposed into two individual Lorentz components.

XPS measurements were carried out to obtain chemical states of elements regarding the materials. The fitted XPS spectra of the BTNO-21 are shown in Figure 6. The Bi 4f doublets ($4f_{5/2}$ and $4f_{7/2}$) consist of two peaks located at 164.4 eV and 159.1 eV. Similarly, the two peaks of Nb 3d at 208.9 eV and 206.2 eV are attributed to the $3d_{3/2}$ and $3d_{5/2}$, respectively. According to the reported binding energies with valance states, the fitted results suggest a "+3" valance of Bi and "+5" valance of Nb in the BTNO-21 [24]. Because the dipole 2p-3d transition of the titanium, spin-orbit splitting of the Ti 2p orbitals into $2p_{3/2}$ and $2p_{1/2}$, and crystal field splitting of the Ti 3d orbitals into e_g and t_{2g}, generally result in three or four peaks for the Ti XPS spectrum [25]. Therefore, the peaks at 457.7 eV, 463.2 eV and 465.6 eV (Sat) belong to the $2p_{3/2}$, $2p_{1/2}$ and e_g, respectively, implying that the Ti ions in the sample have a "+4" valance state. The O 1s signal can be fitted as two peaks at 529.5 eV and 530.3 eV, which may be attributed to lattice oxygen and oxygen vacancies, respectively [26]. The existence of the oxygen vacancies means the possibility of dielectric relaxation, because of their thermally activated movement, which in fact was consistent with the dielectric results as described below.

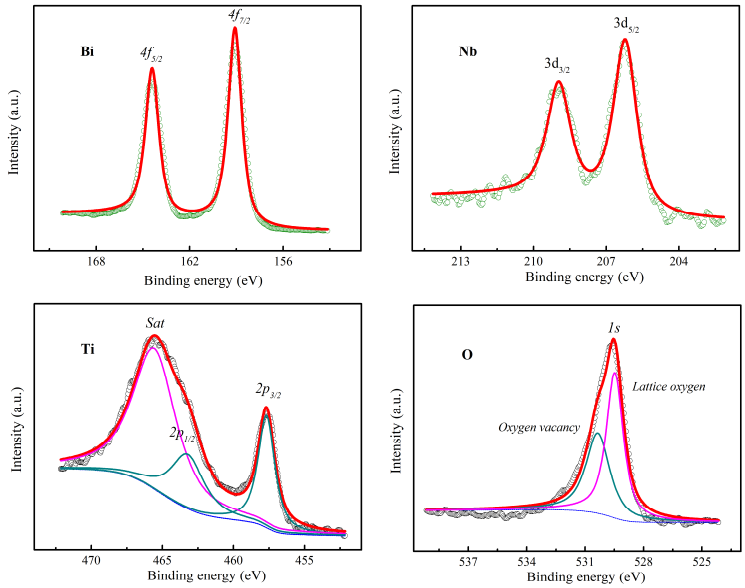

Figure 6. The original and fitted X-ray Photoelectron Spectroscopy (XPS) spectra of Bi 4f, Nb 3d, Ti 2p and O 1s for BTNO-21.

3.3. Ferroelectric and Dielectric Properties

The room-temperature ferroelectric hysteresis loops of the BTN-9, BTNO-21 and BTO−12 ceramics were measured using "top-bottom" Ag-electrodes under different frequencies and electric fields. The P-E loops of the samples measured at 50 Hz under applied 60~130 kV/cm are shown in Figure 7a–c. Even though the applied electric field (E) was not enough to saturate the loops due to the ceramic's leak or breakdown, the P-E loops still reflected clear ferroelectricity in the three samples. With increasing E, the P-E loop was well improved and the typical ferroelectric hysteresis loop was obtained under 120 kV/cm in the BTNO-21(Figure 7b). The remnant polarization ($2P_r$) and coercive field ($2E_c$) are about 12.8 μC/cm^2 and 104 kV/cm, respectively, which are higher than the previously reported values, such as Co-doped $Bi_7Ti_4NbO_{21}$ reported by Liu et al., 2.57–9.33 μC/cm^2 at 150 kV/cm [27] and Nd-doped $Bi_7Ti_4NbO_{21}$ reported by Shao et al., 8 μC/cm^2 at 135 kV/cm [28]. More importantly, the P-E loops of the BTNO-21 are better than those of the BTN-9 (Figure 7a) and BTO−12 (Figure 7c), indicating that the ferroelectric polarization of the mixed-layer structure with engineered interfaces is higher than that of the homologous-phase structure.

To identify the polarization contribution from leakage, the P-E loops at 10 and 50 Hz and remnant-only polarization hysteresis loop measurements for BTNO-21 were performed and are shown in Figure 7d,e, respectively. Similarly, the results of the BTN-9 are also shown in Figure 7f. The $2P_r$ of the BTNO-21 was slightly enhanced with decreasing the frequency from 50 Hz to 10 Hz, while the $2P_r$ of the BTN-9 improved obviously. Observing the remnant-only loops shown in Figure 7e,f, a well-closed loop was only obtained in the BTNO-21, indicating that the material's polarization is an intrinsic and has a good memory feature. These observed results clarify that Aurivillius-type layered ferroelectrics owning layer-stacked interfaces engineered by the two different layers can enable superior intrinsic ferroelectric polarizations and low-level leakage, compared to the adjacent homologous-type layered ferroelectrics. Further, we compared the ferroelectric performance of BTNO-21 with a representative selection of the previous works, as listed in Table 1. The results reveal that the BTNO-21 ceramic is a promising candidate with superior ferroelectric performance.

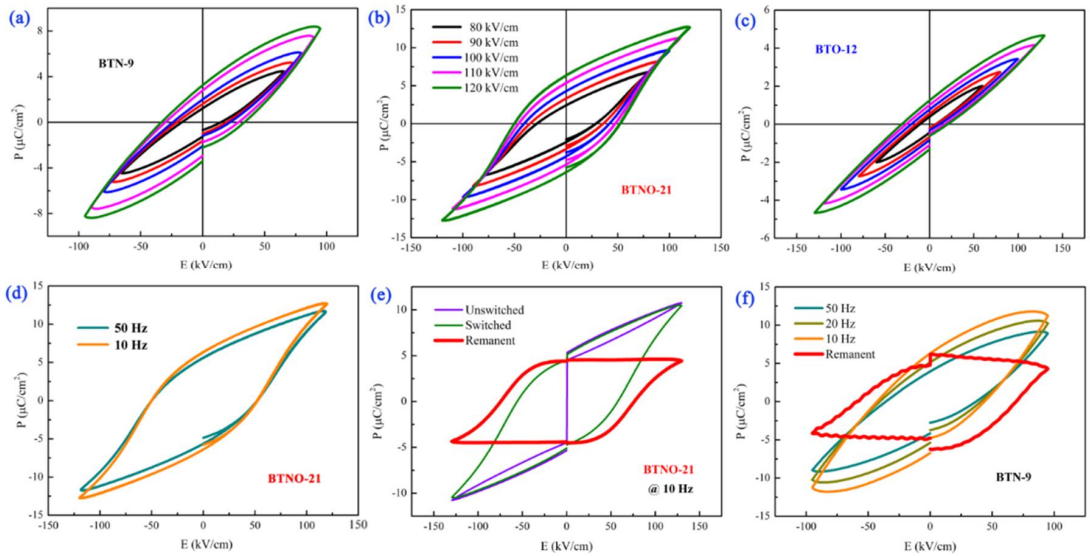

Figure 7. Room-temperature P-E hysteresis loops of (**a**) BTN-9, (**b**) BTNO-21 and (**c**) BTO−12 ceramics; (**d**) BTNO-21's frequency dependence of P-E hysteresis loops under 120 kV/cm; (**e**) Room-temperature remnant-only polarization hysteresis loop for BTNO-21 at 10 Hz; (**f**) P-E hysteresis loops of the BTN-9 at different frequencies and its remnant-only polarization hysteresis loop at 10 Hz.

Figure 8 shows the BTNO-21's relative permittivity (ε′) and dielectric loss (tan δ) as a function of temperature (100–700 °C) and frequency (200–50000 Hz). The ε′ first increased slowly as temperature increased from 100 to 400 °C and then showed an abrupt increase with further increasing temperature. A broad dielectric peak which shifted toward higher temperatures accompanied by a decrease in its height as the frequency increased was clearly observed at 200–400 °C, as shown in Figure 8a. This is a frequency-dependent relaxation behavior in the ceramic. In fact, the similar dielectric behavior was also observed in high-layer Aurivillius-type oxide ceramics and the proposed mechanism was the thermally activated polarization behaviors of charges such as space charges, charged defects and so on [29]. Above 600 °C, the ε′ increased dramatically with increasing the testing temperature, however, the dielectric peak related to the transition from ferroelectric to paraelectric phases was not observed, implying a high Curie temperature. This suggests that the layer-stacked interface engineering inside Aurivillius-type layered structure still remains the relatively high ferroelectric Curie temperature. In Figure 8b, the loss relaxation was found at 400–700 °C and exhibited a strong frequency dispersion. This relaxation is a typical characteristic of relaxor-ferroelectrics ascribed to a thermally activated process [30]. Thereby, the variation of the temperature of the loss peak at different frequencies can be fit by the Arrhenius law. The obtained activation energy was ~2.31 eV, which is very close to 2.3 eV for $Bi_4Ti_3O_{12}$ reported by Jimenez et al. [31] ascribed to the long-range migration of oxygen vacancies.

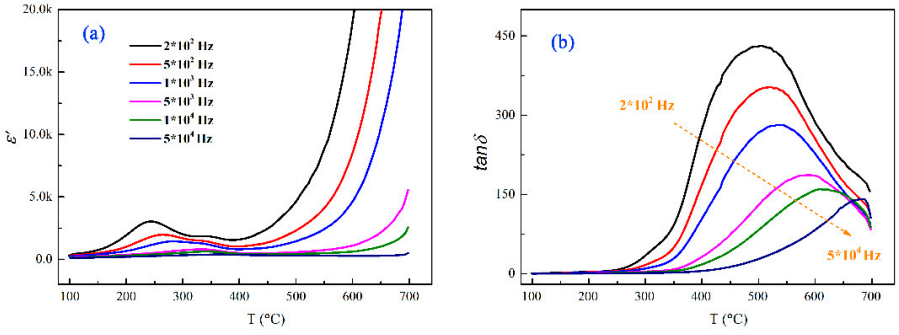

Figure 8. High-temperature dielectric responses of the BTNO-21 ceramic. Temperature dependence of (**a**) relative permittivity ε′ and (**b**) dielectric loss tan δ at different frequencies.

Table 1. Ferroelectric and dielectric properties of the materials reported recently (to be compared with this work).

Materials	$2P_r$ ($\mu C/cm^2$)	$2E_c$ (kV/cm)	Applied E (kV/cm)	Curie Temperature (K)	Activation Energy (eV)	Ref.
$Bi_{1.5}Sr_{0.5}Ti_{1.5}Nb_{0.5}O_7$ ceramic (pyrochlore-phase)	11.4	92	100	>473	1.75	[32]
$BiFeO_3$ ceramic	8.9	78	100	1103	––	[33]
Bi_3TiNbO_9 textured ceramic (2-layer)	1–13.6	120	100	1187	––	[34]
$Bi_4Ti_3O_{12}$ oriented ceramic (3-layer)	4.5–50	10–100	>30	948	2.3	[35]
$Bi_5FeTi_3O_{15}$ ceramic (4-layer)	9.7	202	230	1013	0.67	[36]
$Gd_{0.75}Bi_{4.25}Fe_{0.5}Co_{0.5}Ti_3O_{15}$ ceramic (4-layer)	10.6	200	180	1072	0.84	[37]
$Bi_{11}Fe_3Ti_6O_{33}$ ceramic (mixed-layer)	4.7	110	130	992	––	[15]
BTNO-21 ceramic (mixed-layer)	12.8	104	120	>1000	2.31	This work

3.4. Correlations Between Structures and Properties

In the layered perovskite phase, the ubiquitous oxygen octahedral rotations play an important role in determining structural and physicochemical functionalities [38]. Accordingly, the larger ferroelectric response of the BTNO-21 with the mixed-layer structure can strongly relate to lattice distortions such as rotations, tilts, stretching and bending. To exhibit structural distortions from the atomic structures, the HAADF-STEM image of the "2-3-2-3-2-3-2" layered structure is shown in Figure 9. To determine clear atom positions, the maps of the brightness scanned along three lines are also shown in Figure 9. Detailed analysis of these images suggested the existence of the obvious shift of the B-site atoms along the c-axis in the perovskite slabs. The calculated distances between the adjacent Bi-atom layers were ~0.474–0.453–0.475 nm for the 3-layer structure and ~0.495–0.495 nm for the 2-layer structure. Lomanova et al. [39] reported the cell parameter c in the Aurivillius-type oxides raised almost linearly as n increased and the best fit straight line was $c = 8.22\ n + 8.16$. Jiang et al. [24] reported that the parameter c refined by the Rietveld method in the BTN-9 was 2.51 nm. Therefore, the ideal distance of the Bi-Bi layer in the BTN-9 is about 0.42 nm. Meanwhile, in the BTNO-21 compound, the distance of 0.495 nm shows a larger stretching, probably arising from the nearly uniform distributing of the Nb atoms in the 2-layer and 3-layer slabs giving rise to different strain states at the layer-stacked interfaces or from the interfacial polar interactions. This observation implies that complicated lattice deformations, for instance, Jahn–Teller distortions, stretching/bending/bucking distortions and octahedral rotations [40,41] may seriously exist near the layer-stacked interfaces engineered by the different layer slabs. Therefore, the superior ferroelectric property of the BTNO-21 sample compared with the other samples could be explained by the intrinsic mixed-layer structure, convinced by reasons as follows: (1) the breaking of the inversion symmetry may induce larger spontaneous polarization along *a*-axis and *c*-axis simultaneously; (2) perovskite distortions near the layer-stacked interfaces may produce a polar structure, for example ($a^-a^-c^+$)-type tilts coupled with broken translational symmetry could generate some additional ferroelectricity [42]; (3) the distributing of the Nb atoms in the 3-layer perovskite slabs equals the partial Nb-substitution on the Ti-sites, enhancing the spontaneous polarization from the 3-layer perovskite slabs.

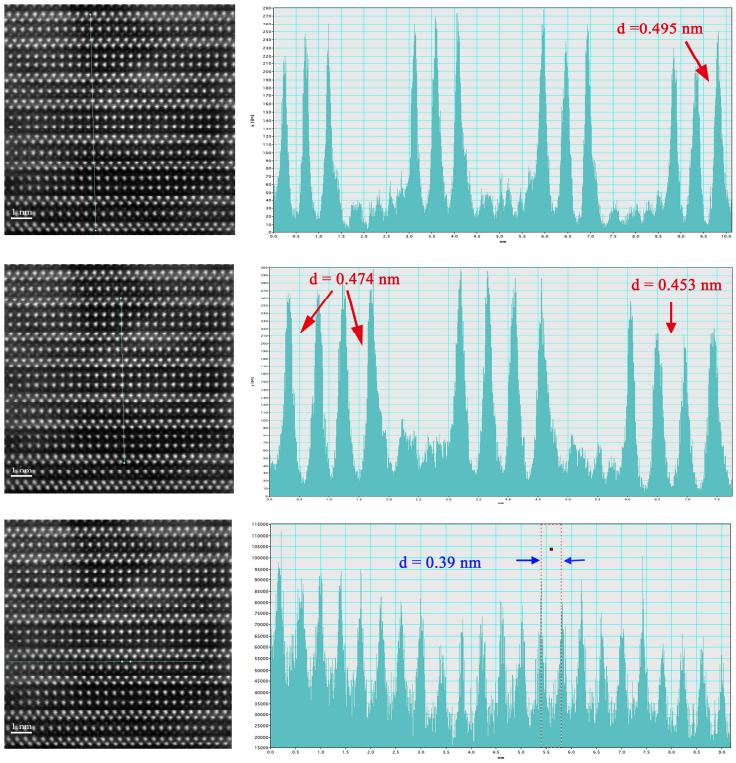

Figure 9. Representative STEM-HAADF image of the BTNO-21 and the three maps of the brightness scanned along three lines.

4. Conclusions

In summary, layer-stacked interfaces engineered by the different layer slabs inside the Aurivillius-type structure were exploited, representing a reliable method to tailor the physical properties. We demonstrated its effect on the analysis of the BTNO-21 synthesized using the solid-state reactions from BTN-9 and BTO−12 powder mixtures. As a result, the ordered intergrowth structure of the 2-layer and 3-layer perovskite slabs sandwiched between the Bi-O layers in the single-phase BTNO-21, metal element distributing and lattice distortions were visualized. The enhanced ferroelectric property of the BTNO-21 sample compared with the other samples was recorded. Analyses of the Raman spectra, XPS and atomic structures confirmed that this improved performance could be correlated with the engineered layer-stacked interface inside the Aurivillius-type layered-structure, arising from the combined effect of the broken symmetry, strain-induced distortions near the correlated interfaces and interfacial polar interactions.

Author Contributions: S.S. wrote the original draft, S.S. and X.Y. performed the experimental work. X.Y. revised the paper and gave useful suggestions. All authors contributed to the general discussion. All authors have read and agreed to the published version of the manuscript.

Funding: The work was financially supported by the National Natural Science Foundation of China (No. 51702276), the Key Technologies R&D Program of Henan Province (Grant No.182102210133), and the Key Project of Henan Province Colleges and Universities Plan (No. 18A140030, 19A430021).

Acknowledgments: S.S. acknowledges the support from the Nanhu Scholars Program for Young Scholars of XYNU.

Conflicts of Interest: The authors declare no conflict of interest.

References

1. Hwang, H.Y.; Lwasa, Y.; Kawasaki, M.; Keimer, B.; Nagaosa, N.; Tokura, Y. Emergent phenomena at oxide interfaces. *Nat. Mater.* **2012**, *11*, 103–113.
2. Dong, H.; Xu, F.; Sun, Z.Q.; Wu, X.; Zhang, Q.B.; Zhai, Y.S.; Tan, X.D.; He, L.; Xu, T.; Zhang, Z.; et al. In situ interface engineering for probing the limit of quantum dot photovoltaic devices. *Nat. Nanotechnol.* **2019**, *14*, 950–956.
3. Spaldin, N.A.; Ramesh, R. Advances in magnetoelectric multiferroics. *Nat. Mater.* **2019**, *18*, 103–113.
4. Cao, Y.; Li, W.W.; Liu, Z.; Zhao, Z.Q.; Xiao, Z.Y.; Zi, W.; Cheng, N. Ligand modification of Cu_2ZnSnS_4 nanoparticles boosts the performance of low temperature paintable carbon electrode based perovskite solar cells to 17.71%. *J. Mater. Chem. A* **2020**, *8*, 12080–12088.
5. Mundy, J.; Brooks, C.; Holtz, M.; Moyer, J.; Das, H.; Rebola, A.; Heron, J.; Clarkson, J.; Disseler, S.; Liu, Z.; et al. Atomically engineered ferroic layers yield a room-temperature magnetoelectric multiferroic. *Nature* **2016**, *537*, 523–527.
6. Anderson, P.W. More is different. *Science* **1972**, *177*, 393–396.
7. Fiebig, M.; Lottermoser, T.; Meier, D.; Trassin, M. The evolution of multiferroics. *Nat. Rev. Mater.* **2016**, *1*, 16046.
8. Gopalan, V.; Engel-Herbert, R. Creative tension in layered crystals. *Nat. Mater.* **2016**, *15*, 928–930.
9. Moure, A. Review and perspectives of Aurivillius structures as a lead-free piezoelectric system. *Appl. Sci.* **2018**, *8*, 62.
10. Chon, U.; Jang, H.M.; Kim, M.G.; Chang, C.H. Layered perovskites with giant spontaneous polarizations for nonvolatile memories. *Phys. Rev. Lett.* **2002**, *89*, 087601.
11. Lisiñska-Czekaj, A.; Czekaj, D.; Gomes, M.; Kuprianov, M. Investigations on the synthesis of Bi_3NbTiO_9 ceramics. *J. Eur. Ceram. Soc.* **1999**, *19*, 969–972.
12. Lei, Z.; Chen, T.; Li, W.; Liu, M.; Ge, W.; Lu, Y. Cobalt-substituted seven-layer Aurivillius $Bi_8Fe_4Ti_3O_{24}$ ceramics: Enhanced ferromagnetism and ferroelectricity. *Crystals* **2017**, *7*, 76.
13. Krzhizhanovskaya, M.; Filatov, S.; Gusarov, V.; Paufler, P.; Bubnova, R.; Morozov, M.; Meyer, D.C. Aurivillius phases in the $Bi_4Ti_3O_{12}/BiFeO_3$ system: Termal behaviour and crystal structure. *Z Anorg. Allg. Chem.* **2005**, *631*, 1603–1608.
14. Sun, S.J.; Huang, Y.; Wang, G.P.; Wang, J.L.; Peng, R.R.; Fu, Z.P.; Zhai, X.F.; Mao, X.Y.; Chen, X.B.; Lu, Y.L. Room-temperature multiferroic responses arising from 1D phase modulation in correlated Aurivillius-type layer structures. *J. Phys. D Appl. Phys.* **2016**, *49*, 125005.
15. Sun, S.J.; Liu, C.H.; Wang, G.P.; Chen, Z.Z.; Chen, T.; Peng, R.R.; Lu, Y.L. Structural and physical properties of mixed-layer Aurivillius-type multiferroics. *J. Am. Ceram. Soc.* **2016**, *99*, 3033–3038.
16. Sun, S.J.; Huang, Y.; Wang, G.P.; Wang, J.L.; Fu, Z.P.; Peng, R.R.; Knize, R.J.; Lu, Y.L. Nanoscale structural modulation and enhanced room-temperature multiferroic properties. *Nanoscale* **2014**, *6*, 13494–13500.
17. Sun, S.J.; Chen, Z.Z.; Wang, G.P.; Geng, X.J.; Xiao, Z.Y.; Sun, Z.Z.; Sun, Z.H.; Peng, R.R.; Lu, Y.L. Nanoscale structural modulation and low-temperature magnetic response in mixed-layer Aurivillius-type oxides. *Sci. Rep.* **2018**, *8*, 871.
18. Wang, G.P.; Chen, Z.Z.; He, H.C.; Meng, D.C.; Yang, H.; Mao, X.Y.; Pan, Q.; Chu, B.J.; Zuo, M.; Sun, Z.H.; et al. Room temperature exchange bias in structure-modulated single-phase multiferroic materials. *Chem. Mater.* **2018**, *30*, 6156–6163.
19. Faraz, A.; Arif, S. Magnetic-field-induced ferroelectric domain dynamics and in-plane polarization in odd and mixed layered Aurivillius structures. *J. Appl. Phys.* **2019**, *126*, 084104.
20. Keeney, L.; Downing, C.; Schmidt, M.; Pemble, M.E.; Nicolosi, V.; Whatmore, R.W. Direct atomic scale determination of magnetic ion partition in a room temperature multiferroic material. *Sci. Rep.* **2017**, *7*, 1737.
21. Morozov, M.I.; Gusarov, V.V. Synthesis of $A_{m-1}Bi_2M_mO_{3m+3}$ compounds in the $Bi_4Ti_3O_{12}$–$BiFeO_3$ system. *Inorg. Mater.* **2002**, *38*, 723–729.
22. Arenas, D.J.; Gasparov, L.V.; Qiu, W.; Nino, J.C.; Patterson, C.H.; Tanner, D.B. Raman study of phonon modes in bismuth pyrochlores. *Phys. Rev. B* **2010**, *82*, 214302.
23. Kojima, S.; Imaizumi, R.; Hamazaki, S.; Takashige, M. Raman scattering study of bismuth layer-structure ferroelectrics. *Jpn. J. Appl. Phys.* **1994**, *33*, 5559–5564.

24. Jiang, L.; Ni, S.; Liu, G.; Xu, X. Photocatalytic hydrogen production over Aurivillius compound Bi_3TiNbO_9 and its modifications by Cr/Nb co-doping. *Appl. Catal. B Environ.* **2017**, *217*, 342–352.
25. Kaspar, T.C.; Ney, A.; Mangham, A.N.; Heald, S.M.; Joly, Y.; Ney, V.; Wilhelm, F.; Rogalev, A.; Yakou, F.; Chambers, S.A. Structure of epitaxial (Fe,N) codoped rutile TiO_2 thin films by x-ray absorption. *Phys. Rev. B* **2012**, *86*, 3089–3094.
26. Sun, S.; Zhu, L.; Zhang, B.; Zhang, L.; Li, Y.; Cheng, N.; Yin, X.; Tian, Y.; Li, X.; Lu, Y. Structural modulation enables magneto-dielectric effect and enhanced photoactivity in ferroelectric bismuth iron niobate pyrochlore. *J. Mater. Chem. C* **2019**, *7*, 1263–1272.
27. Liu, C.H.; Chen, Z.Z.; Peng, R.R.; Fu, Z.P.; Zhai, X.F.; Lu, Y.L. The structure and properties of Co substituted $Bi_7Ti_4NbO_{21}$ with intergrowth phases. *RSC Adv.* **2017**, *7*, 50477.
28. Shao, C.; Lu, Y.; Wang, D.; Li, Y. Effect of Nd substitution on the microstructure and electrical properties of $Bi_7Ti_4NbO_{21}$ piezoceramics. *J. Eur. Ceram. Soc.* **2012**, *32*, 3781–3789.
29. Rehman, F.; Wang, L.; Jin, H.B.; Ahmad, P.; Zhao, Y.J.; Li, J.B. Dielectric relaxation and electrical properties of $Sm_{0.5}Bi_{4.5}Ti_3FeO_{15}$ ceramics. *J. Alloy Compd.* **2017**, *709*, 686–691.
30. Sun, S.J.; Chen, W.J.; Fang, L.; Cheng, N.; Xiao, Z.Y.; Zhao, Z.Q.; Tian, Y.S.; Lu, Y.L. Dielectric relaxation and microwave absorption properties of aurivillius-type multiferroic ceramics. *Ceram. Int.* **2018**, *44*, 9942–9949.
31. Jimenez, B.; Jimenez, R.; Castro, A.; Millan, P.; Pardo, L. Dielectric and mechanoelastic relaxations due to point defects in layered bismuth titanate ceramics. *J. Phys. Condens. Matter.* **2001**, *13*, 7315–7326.
32. Du, H.L.; Shi, X. Strontium-induced ferroelectriclike relaxor behavior in Bi-based pyrochlores. *Appl. Phys. Lett.* **2010**, *97*, 052901.
33. Rojac, T.; Bencan, A.; Malic, B.; Tutuncu, G.; Jones, J.L.; Daniels, J.E.; Damjanovic, D. $BiFeO_3$ ceramics: Processing, electrical, and electromechanical properties. *J. Am. Ceram. Soc.* **2014**, *97*, 1993–2011.
34. Zhou, Z.Y.; Li, Y.C.; Yang, L.H.; Dong, X.L.; Wang, Y.L. Microstructure and electrical properties of textured Bi-Layered Bi_3TiNbO_9 piezoceramics. *Ferroelectrics* **2008**, *363*, 127–133.
35. Kong, L.B.; Ma, J.; Zhu, W.; Tan, O.K. Preparation of $Bi_4Ti_3O_{12}$ ceramics via a high-energy ball milling process. *Mater. Lett.* **2001**, *51*, 108–114.
36. Mao, X.; Sun, H.; Wang, W.; Lu, Y.L.; Chen, X.B. Effects of Co-substitutes on multiferroic properties of $Bi_5FeTi_3O_{15}$ ceramics. *Solid State Commun.* **2012**, *152*, 483–487.
37. Wu, Y.Y.; Yao, T.S.; Lu, Y.X.; Zou, B.W.; Mao, X.Y.; Huang, F.Z.; Sun, H.; Chen, X.B. Magnetic, dielectric, and magnetodielectric properties of Bi-layered perovskite $Bi_{4.25}Gd_{0.75}Fe_{0.5}Co_{0.5}Ti_3O_{15}$. *J. Mater. Sci.* **2017**, *52*, 7360–7368.
38. Glazer, A. The classification of tilted octahedra in perovskites. *Acta Crystallogr. B* **1972**, *28*, 3384–3392.
39. Lomanova, N.A.; Morozov, M.I.; Ugolkov, V.L.; Gusarov, V.V. Properties of Aurivillius phases in the $Bi_4Ti_3O_{12}$-$BiFeO_3$ system. *Inorg. Mater.* **2006**, *42*, 189–195.
40. He, J.; Borisevich, A.; Kalinin, S.V.; Pennycook, S.J.; Pantelides, S.T. Control of octahedral tilts and magnetic properties of perovskite oxide heterostructures by substrate symmetry. *Phys. Rev. Lett.* **2010**, *105*, 227203.
41. Zhai, X.F.; Long, C.; Liu, Y.; Schleputz, C.M.; Dong, S.; Li, H.; Zhang, X.Q.; Chu, S.Q.; Zheng, L.R.; Zhang, J.; et al. Correlating interfacial octahedral rotations with magnetism in $(LaMnO_{3+\delta})N/(SrTiO_3)N$ superlattices. *Nat. Commun.* **2014**, *5*, 4283.
42. Pitcher, M.J.; Mandal, P.; Dyer, M.S.; Alaria, J.; Borisov, P.; Niu, H.; Claridge, J.B.; Rosseinsky, M.J. Tilt engineering of spontaneous polarization and magnetization above 300 K in a bulk layered perovskite. *Science* **2015**, *374*, 420–424.

© 2020 by the authors. Licensee MDPI, Basel, Switzerland. This article is an open access article distributed under the terms and conditions of the Creative Commons Attribution (CC BY) license (http://creativecommons.org/licenses/by/4.0/).